

On the Surface Fields Excited by a Hertzian Dipole Over a Layered Halfspace: From Radio to Optical Wavelengths

Krzysztof A. Michalski, *Fellow, IEEE*, and Juan R. Mosig, *Fellow, IEEE*

Dedicated to Professor Chalmers M. Butler on the occasion of his 80th birthday

Abstract—The Sommerfeld halfspace problem is revisited allowing for multilayer and plasmonic media, with a focus on the surface field computation. Alternative field representations are discussed and an improved Sommerfeld–Norton groundwave formula is developed. The role of the Zenneck wave and surface plasmon polariton in the surface field and their relationship is elucidated. The theoretical development is illustrated and validated by representative numerical results.

Index Terms—Sommerfeld–Norton groundwave, surface plasmon polariton (SPP), surface wave, Zenneck wave (ZW).

I. INTRODUCTION

RECENTLY, there has been a resurgence of interest in the Sommerfeld halfspace problem [1] in the context of high-frequency (HF) maritime radar [2], HF wireless communications [3], ground-penetrating radar (GPR) [4], as well as in terahertz [5], near-field optics [6], and plasmonic/nanophotonic applications [7], where electromagnetic fields propagating along the surface are of paramount importance. In his seminal 1909 paper, Sommerfeld presented the first rigorous solution for a vertical Hertzian dipole above a lossy ground, expressed in terms of Fourier–Bessel transforms—which are still commonly referred to as Sommerfeld integrals. Sommerfeld also extended the integration path of the Fourier–Bessel transform to the whole real axis and wrapped it around the fundamental branch cuts and the pole of the integrand—the Sommerfeld pole, which gives rise to the cylindrical Zenneck wave (ZW) [8]—and thus, converted the axial-transmission representation of the solution to the radial-transmission representation [9]. The latter makes the associated physical phenomena more evident and Sommerfeld used it as the point of departure in the derivation of a closed-form asymptotic expansion of the surface field

far from the dipole, assuming high-media contrast.¹ The same problem was shortly thereafter treated by Weyl [13] (using a new and ingenious method) and again by Sommerfeld [12] (see also [14]). Extensions of the Weyl and Sommerfeld formulations to a layered halfspace were later proposed by Grosskopf [15] and Wait [16], [17]. Another important milestone was the “user-friendly” surface wave formula derived by Norton [18] based on an earlier work of van der Pol [19], which is often referred to as the Norton surface wave [20] or the Sommerfeld–Norton groundwave formula [21, p. 97], [22, p. 310]. Perhaps the most recent groundwave formulation is due to King and Sandler [23].²

In this paper, we revisit the classical Sommerfeld halfspace problem with an extension to multilayer media, as illustrated in Fig. 1. We also allow for plasmonic materials, which were not the concern of the early investigations in this area. The focus is on the surface fields when $h/\rho \ll 1$, where h is the height of the dipole above the layered halfspace and ρ is the horizontal distance. Although from the mathematical standpoint the solution of this problem is identical whether at radio frequencies or in the optical regime, and there is a close relationship between the ZW and the surface plasmon polariton (SPP)—as they satisfy the same transverse resonance condition [25]–[27], there are also some important nuances in the way these waves contribute to the surface field. To elucidate these nuances, we discuss alternative field representations—resulting from wrapping the Sommerfeld integration path around the branch-cut and pole singularities in the complex plane. As a byproduct, we also obtain an improved Sommerfeld–Norton groundwave formula. The theoretical development is illustrated and validated by representative numerical results.

II. THEORETICAL DEVELOPMENT

A. Green Functions for the Upper Halfspace

For an arbitrarily oriented Hertzian dipole with the current moment Il , we may find the (magnetic) vector potential as

$$\mathbf{A}(\mathbf{r}) = \underline{\underline{\mathbf{G}}}^A(\mathbf{r}|\mathbf{r}') \cdot Il \quad (1)$$

¹A subtle error in this expression was later uncovered [10], [11], but in the meantime Sommerfeld derived a correct formula when he revisited this problem in 1926 [12]. It should also be noted that Sommerfeld originally placed the dipole in the interface.

²However, this formulation does not properly account for the possible trapped wave [24].

Manuscript received April 23, 2015; revised July 21, 2015; accepted September 24, 2015. Date of publication September 30, 2015; date of current version November 25, 2015. This work was supported by École Polytechnique Fédérale de Lausanne (EPFL), Switzerland.

K. A. Michalski is with the Department of Electrical and Computer Engineering, Texas A&M University, College Station, TX 77843-3128 USA (e-mail: k-michalski@tamu.edu).

J. R. Mosig is with the Laboratory of Electromagnetics and Acoustics, École Polytechnique Fédérale de Lausanne, Lausanne CH-1015, Switzerland (e-mail: juan.mosig@epfl.ch).

Color versions of one or more of the figures in this paper are available online at <http://ieeexplore.ieee.org>.

Digital Object Identifier 10.1109/TAP.2015.2484422

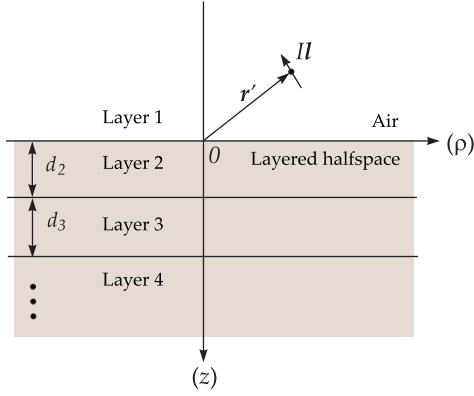


Fig. 1. Dipole source above a layered halfspace.

where

$$\underline{\underline{G}}^A = (\hat{x}\hat{x} + \hat{y}\hat{y})G_{xx}^A + \hat{z}\hat{x}G_{zx}^A + \hat{z}\hat{y}G_{zy}^A + \hat{z}\hat{z}G_{zz}^A \quad (2)$$

is the vector-potential dyadic Green function of the layered medium. The electric and magnetic fields may similarly be found using the corresponding Green dyadics³

$$\underline{\underline{G}}^E = -j\omega \underline{\underline{G}}^A + \frac{1}{j\omega} \nabla \left(\frac{1}{\epsilon} \nabla \cdot \frac{1}{\mu} \underline{\underline{G}}^A \right) \quad (3)$$

and

$$\underline{\underline{G}}^H = \frac{1}{\mu} \nabla \times \underline{\underline{G}}^A \quad (4)$$

where the permittivity ϵ and permeability μ pertain to the observation layer. In the upper half-space (layer 1), the components of the Green dyadic (2) may be expressed as [28]

$$G_{xx}^A = \mu_1 \frac{e^{-jk_1 R}}{4\pi R} + \mu_1 S_0 \left\{ \frac{\vec{I}_1^h}{2jk_{z1}} e^{jk_{z1}(z+z')} \right\} \quad (5)$$

$$G_{zz}^A = \mu_1 \frac{e^{-jk_1 R}}{4\pi R} - \mu_1 S_0 \left\{ \frac{\vec{I}_1^e}{2jk_{z1}} e^{jk_{z1}(z+z')} \right\} \quad (6)$$

$$G_{zx}^A = \cos \phi \mu_1 S_1 \left\{ \frac{\vec{I}_1^h - \vec{I}_1^e}{2k_\rho} e^{jk_{z1}(z+z')} \right\} \quad (7)$$

with G_{zy}^A given by (7) with $\sin \phi$ in place of $\cos \phi$. In the above, we have introduced the notation

$$S_n\{\tilde{f}(k_\rho)\} = \frac{1}{2\pi} \int_0^\infty \tilde{f}(k_\rho) J_n(k_\rho \rho) k_\rho dk_\rho \quad (8)$$

where J_n is the Bessel function of order n . We have also used the Sommerfeld identity [1]

$$S_0 \left\{ \frac{e^{-jk_{z1}|z-z'|}}{2jk_{z1}} \right\} = \frac{e^{-jk_1 R}}{4\pi R}, \quad R = \sqrt{\rho^2 + (z-z')^2} \quad (9)$$

to extract the whole-space terms in a closed form. The spectral integrands $\tilde{f}(k_\rho)$ in the above are readily derived using the transmission-line (TL) network analogue of the layered

medium, in which the planar layers are represented by TL sections [28], [29]. Two TL networks arise, propagating the transverse-magnetic (TM) and transverse-electric (TE) partial fields. The n th layer of the medium is represented by a TL section with the propagation constant

$$k_{zn} = \sqrt{k_n^2 - k_\rho^2}, \quad k_n = \omega \sqrt{\mu_n \epsilon_n} \quad (10)$$

and characteristic impedance Z_n^p , where $p = e$ (TM wave) or h (TE wave), given as

$$Z_n^e = \frac{k_{zn}}{\omega \epsilon_n}, \quad Z_n^h = \frac{\omega \mu_n}{k_{zn}}. \quad (11)$$

The voltage reflection coefficient \vec{I}_1^p looking into the layered halfspace can be found from the recursion (with the superscript p omitted for simplicity)

$$\vec{I}_n = \frac{\vec{r}_n + \vec{I}_{n+1} \Phi_{n+1}^2}{1 + \vec{r}_n \vec{I}_{n+1} \Phi_{n+1}^2}, \quad n = N-1, \dots, 1 \quad (12)$$

with $\vec{I}_N \equiv 0$ and

$$\vec{r}_n = \frac{Z_{n+1} - Z_n}{Z_{n+1} + Z_n}, \quad \Phi_n = e^{-jk_{zn} d_n} \quad (13)$$

where d_n is the thickness of layer n .

The upper halfspace Green functions may also be expressed in alternative forms by extracting from the Sommerfeld integrals an image term in a planar mirror made of either perfect-electric conductor (PEC) or perfect-magnetic conductor (PMC). For example, upon extracting the PMC image and using the Sommerfeld identity (9), we may express (6) as [18], [30]

$$G_{zz}^A = \frac{\mu_1}{4\pi} \left(\frac{e^{-jk_1 R}}{R} - \frac{e^{-jk_1 R^*}}{R^*} + 4\pi S_0 \left\{ \frac{1 - \vec{I}_1^e}{2jk_{z1}} e^{jk_{z1}(z+z')} \right\} \right) \quad (14)$$

where $R^* = \sqrt{\rho^2 + (z+z')^2}$. In this form, the direct (whole-space) and image terms cancel at the interface $z = 0$, leaving the Sommerfeld integral term as the sole contribution [24].

B. Integrand Singularities

The integrands in (5)–(7) and (14) comprise the propagation constants k_{zn} defined by the square root function (10), which is double-valued with branch points at $k_\rho = \pm k_n$ [31, p. 57], [32, App. B], [33, Sec. 1–6]. For a unique specification of this square root in the complex k_ρ -plane, we impose the condition $\Im m k_{zn} \leq 0$, which defines a two-sheeted Riemann surface with hyperbolic (or fundamental) branch cuts in the second and fourth quadrants. We refer to the sheet on which the condition $\Im m k_{zn} \leq 0$ is satisfied as the *proper sheet*, and the sheet on which this condition does not hold as the *improper sheet*. This nomenclature derives from the fact that on the proper sheet, the function $e^{-jk_{zn} z}$ satisfies the *radiation condition* at infinity, i.e.,

³The $e^{j\omega t}$ time convention is implied.

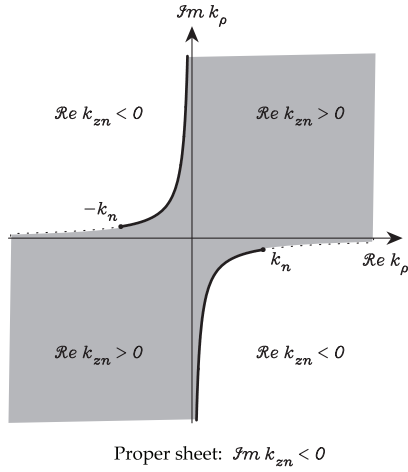


Fig. 2. Proper Riemann sheet associated with $k_{zn} = \sqrt{k_n^2 - k_p^2}$.

it vanishes as $z \rightarrow \infty$.⁴ The proper Riemann sheet with fundamental branch cuts is illustrated for a lossy medium in Fig. 2, where the only way to pass from one sheet to another is by crossing one of the branch cuts, on which $\Im m k_{zn} = 0$. Note that $\Re e k_{zn} = 0$ on the hyperbolic extensions of the branch cuts, indicated by the dotted lines. On the improper sheet (not shown for brevity), where $\Im m k_{zn} > 0$, the shaded areas with $\Re e k_{zn} > 0$ are complementary to those shown in Fig. 2. With the exception of active [34] and double-negative media [35], the branch point $k_n = k'_n - jk''_n$ is always located in the fourth quadrant. In the lossless limit, as $k''_n \rightarrow 0$, k_n approaches the positive-real axis and the hyperbolic branch cuts collapse on the real and imaginary axes. The choice of branch cuts is wholly arbitrary, as long as they do not cross the real axis path of the Sommerfeld integrals. The convenience of the fundamental branch cuts is that the radiation condition is satisfied—or not—on an *entire* sheet of the Riemann surface. However, there are instances where *vertical cuts* outgoing from the branch points $\pm k_n$ are preferable—even though the spectral integrands are no longer bounded for *all* values of k_p on the top sheet [30], [31, p. 55], [36, p. 251], [37]. In the case of a layered halfspace, the integrands are even functions of k_{zn} associated with the *finite-thickness* layers, hence $\pm k_1$ and $\pm k_N$ are the only branch points. The integrands in (5)–(7) and (14) may thus be viewed as defined on a four-sheeted Riemann surface, depicted schematically in Fig. 3, where the vertical line segments represent the branch cuts and offer a passage between the sheets [31, p. 56], [35], [38, p. 613].

In addition to the branch points, the spectral integrands have poles, which may be found from the *transverse resonance condition* [39, Sec. 3.6]

$$\mathcal{D}^p(k_p) = \vec{Z}_1^p + Z_1^p = \frac{2Z_1^p}{1 - \vec{Z}_1^p} = 0 \quad (15)$$

where \vec{Z}_1^p is the impedance looking into the layered halfspace. The dispersion function (15) is also defined over the four-sheeted Riemann surface and can have roots on any of

⁴Here a lossless medium should be treated as a limit of the corresponding lossy medium as losses approach zero.

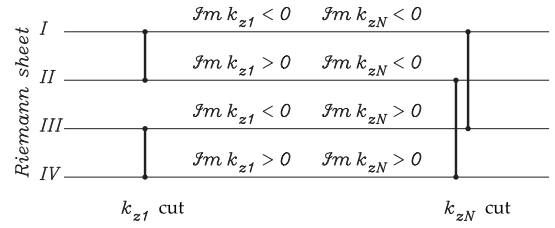


Fig. 3. Schematic diagram of the four-sheeted Riemann surface with fundamental branch cuts associated with k_{z1} and k_{zN} .

the sheets [40]. However, only those located on the top sheet are *proper* and are termed *surface-wave* poles; the ones on the other sheets are *improper* and are termed *leaky-wave* poles. For a *homogeneous* lower halfspace, $\vec{Z}_1^p = Z_2^p$ in (15) and—assuming nonmagnetic media and TM case—it is readily shown that this dispersion function has two roots $\pm k_p$, where

$$k_p = k_1 \sqrt{\frac{\epsilon_r}{\epsilon_r + 1}}, \quad \epsilon_r = \epsilon_2/\epsilon_1 = \epsilon' - j\epsilon'' \quad (16)$$

This pole is located in the fourth-quadrant of the topmost Riemann sheet, as first demonstrated by Sommerfeld [1], [14]. Note that in the high-contrast case ($|\epsilon_r| \gg 1$), which arises in many important applications, this pole may be arbitrarily close to the branch point k_1 . Further, k_p is located to the left or to the right of a vertical cut emanating from k_1 , depending on the sign of ϵ' . For convenience, we will distinguish between the Sommerfeld case—where the pole is to the left of k_1 and the associated ZW is a fast wave, as its phase velocity exceeds the speed of light,⁵ and the plasmonic case—where the pole is to the right of k_1 , and the associated SPP is a slow wave.

In the multilayer case, the poles can only be determined by a numerical search for the roots of the dispersion function (15) in the complex k_p -plane. The most effective root location methods are based on Cauchy's theorem—which, however, requires that the dispersion function be analytic [43]–[45]. Consequently, the branch points are first removed by a suitable mapping $k_p \mapsto \varpi$, which *unfolds* the four-sheeted Riemann surface [46]–[48], and the search is performed in the ϖ -plane.⁶ Further details are outside the intended scope of this paper.

C. Alternative Representations

On the topmost *Sheet I* of the four-sheeted Riemann surface of Fig. 3, the integrands satisfy the radiation condition at infinity and the Sommerfeld integrals are guaranteed to converge. The integration path in (5)–(7) and (14), often referred to as the Sommerfeld integration path (SIP), is thus taken along the positive-real axis on *Sheet I*. However, SIP becomes inefficient for the large ρ values of interest in surface wave investigations,

⁵The group velocity of the ZW can also be greater than the speed of light, which prompted some authors to call it a “mathematical ghost wave” [41]. However, its energy transport velocity never exceeds the speed of light, hence no laws of physics are violated [42].

⁶When $k_N = k_1$, or the layered stack is backed by a PEC or PMC, there is only one pair of branch points $k_p = \pm k_1$, which can be removed by the simple mapping $k_p = k_1 \sin \varpi$ [49]. Alternatively, the search may be performed in the k_{z1} -plane.

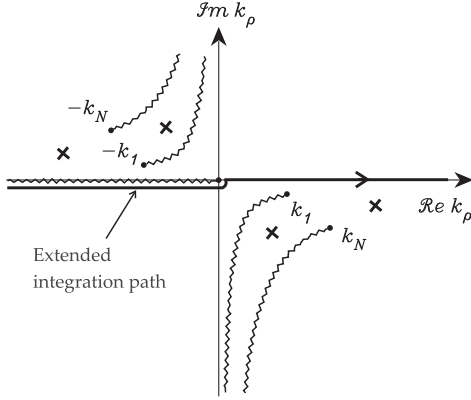


Fig. 4. Extended integration path and representative poles on the top sheet of the Riemann surface associated with k_{z1} and k_{zN} .

due to the rapid oscillations of the Bessel functions. In this case, more efficient integral representations can be obtained by a suitable deformation of the integration path and analytic continuation of integrand functions into the complex k_ρ -plane. However, in order to make the integration path deformable, we must first extend it to the whole real axis. The desired form [1] is achieved by first expressing the Bessel function in (8) in terms of the Hankel functions using [50]

$$J_n(z) = \frac{1}{2} [H_n^{(1)}(z) + H_n^{(2)}(z)] \quad (17)$$

then introducing in the integrand containing $H_n^{(1)}(k_\rho \rho)$ the change of variable $k_\rho \rightarrow k_\rho e^{-j\pi}$, and making use of the circuitual relation

$$H_n^{(1)}(z e^{j\pi}) = -e^{-jn\pi} H_n^{(2)}(z) \quad (18)$$

whence

$$4\pi \mathcal{S}_n\{\tilde{f}(k_\rho)\} = \int_{-\infty e^{-j\pi}}^{\infty} \tilde{f}(k_\rho) H_n^{(2)}(k_\rho \rho) k_\rho dk_\rho \quad (19)$$

provided that $\tilde{f}(k_\rho)$ is an even (odd) function of k_ρ for even (odd) order n . Since the Hankel function introduces an extraneous logarithmic branch point at the origin with a branch cut along the negative-real axis, the extended integration path (EIP) runs just under this branch cut, as illustrated in Fig. 4. Both the SIP and EIP are associated with the axial-transmission representation [9] of the layered medium Green functions. After locating the integrand singularities, it is possible to deform the EIP to obtain the radial-transmission representation [51] (or transverse spectral representation [52]) of the Green functions. Hence, we close the integration path in (19) down by a semi-circular arc at infinity on the topmost Riemann sheet, avoiding the branch point and pole singularities. By Cauchy's theorem, the integral over this closed path is zero. Also, in view of the large-argument form of the Hankel function, viz.

$$H_n^{(2)}(z) \sim \sqrt{\frac{2j}{\pi z}} j^n e^{-jz}, \quad -2\pi < \arg z < \pi \quad (20)$$

the semicircle at infinity contributes nothing to the integral, if $\rho > 0$. Consequently, the real axis path integral in (19) may be

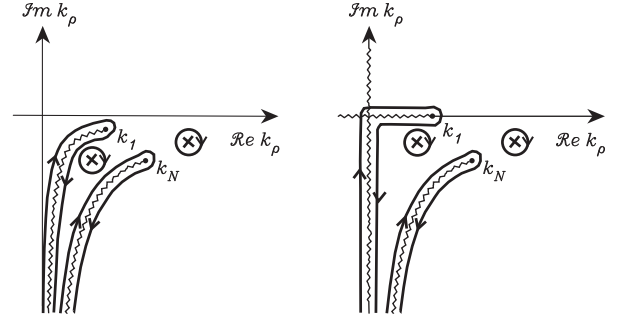


Fig. 5. Integration path wrapped around the poles and fundamental branch cuts for a lossy (left) and lossless (right) upper halfspace.

replaced by integrals around the hyperbolic branch cuts and the residue contributions arising from the presence of the poles, as illustrated in Fig. 5. Note that on the fundamental branch cut associated with k_1 we have $\Im k_{z1} = 0$ and $\Re k_{z1} > 0$, and similarly for the branch cut associated with k_N . It is thus convenient to use the positive-real variables k_{z1} or k_{zN} as the variables of integration on the paths around the two branch cuts in Fig. 5. Using these substitutions, we may express the integral in (19) as

$$\int_{-\infty e^{-j\pi}}^{\infty} \tilde{f}(k_\rho) H_n^{(2)}(k_\rho \rho) k_\rho dk_\rho = \mathcal{Q}_n^1\{\tilde{f}\} + \mathcal{Q}_n^N\{\tilde{f}\} - 2\pi j \sum_i R_{pi} H_n^{(2)}(k_{pi} \rho) k_{pi} \quad (21)$$

where $\mathcal{Q}_n^1\{\tilde{f}\}$ and $\mathcal{Q}_n^N\{\tilde{f}\}$ denote the integrals around the two hyperbolic branch cuts, k_{pi} is the i th pole of $\tilde{f}(k_\rho)$ and R_{pi} is the corresponding residue. The first branch cut integral is given as

$$\mathcal{Q}_n^1\{\tilde{f}\} = \int_0^\infty [\tilde{f}(k_\rho)] H_n^{(2)}(k_\rho \rho) |_{k_\rho = \sqrt{k_1^2 - k_{z1}^2}} k_{z1} dk_{z1} \quad (22)$$

where the $\Im k_\rho < 0$ square root branch should be selected for $k_{z1} > k_1$, and where we have introduced the notation

$$[\tilde{f}(k_\rho)] \equiv \tilde{f}^+(k_\rho) - \tilde{f}^-(k_\rho) \quad (23)$$

for the “folded” spectral integrand function. Here, the plus (minus) superscript on \tilde{f} indicates that every occurrence of k_{z1} is directly replaced by the variable of integration with a plus (minus) sign. The second branch cut integral in (21) is given by (22), except that k_1 is replaced by k_N and the roles of k_{z1} and k_{zN} are interchanged. In the case of moist earth or seawater at radio frequencies, as well as for metals in the optical range, this integral is negligible in comparison with the first branch cut integral, hence we omit further details for brevity. If the upper halfspace is lossless, the branch cut associated with k_1 follows the real and imaginary axes, as indicated in Fig. 5, and we may express $\mathcal{Q}_n^1\{\tilde{f}\}$ as [53, p. 134]

$$\begin{aligned} \mathcal{Q}_n^1\{\tilde{f}\} = & \int_0^{\pi/2} k_1^2 [\tilde{f}(k_\rho)] H_n^{(2)}(k_\rho \rho) |_{k_\rho = k_1 \sin \xi} \sin \xi \cos \xi d\xi \\ & + \frac{2}{\pi} j^{n+1} \int_0^\infty k_1^2 [\tilde{f}(k_\rho)] |_{k_\rho = -jk_1 \xi} K_n(k_1 \rho \xi) \xi d\xi \end{aligned} \quad (24)$$

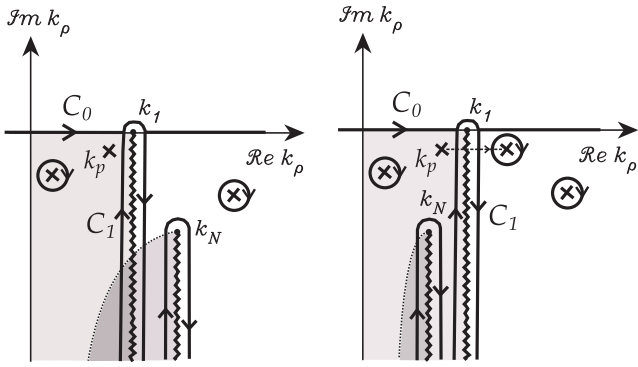


Fig. 6. Integration path wrapped around vertical branch cuts in the case of a lossless upper halfspace. The extended real axis path and the path around the k_1 branch cut are denoted by C_0 and C_1 , respectively. The Sommerfeld pole k_p may cross the vertical branch cut in the plasmonic case. The two situations shown are for $\Re k_N > \Re k_1$ (left) and $\Re k_N < \Re k_1$ (right).

where $[\tilde{f}(k_p)]$ is given in (23), where now the plus (minus) superscript on \tilde{f} indicates that this function should be evaluated on *Riemann Sheet I (II)*. In the first integral above, we made a trigonometric substitution to remove the weak singularity at the branch point k_1 [54], and in the second integral, we used the relationship [50, Eq. (10.27.8)]

$$H_n^{(2)}(-jz) = \frac{2}{\pi} j^{n+1} K_n(z), \quad -\pi/2 < \arg z \leq \pi \quad (25)$$

to express the Hankel function of imaginary argument in terms of the Macdonald function, which is exponentially decreasing.

We next introduce the nonspectral representation⁷ of the integral (19), which has the form

$$\int_{\infty e^{-j\pi}}^{\infty} \tilde{f}(k_p) H_n^{(2)}(k_p \rho) k_p dk_p = \mathcal{I}_n^1 \{ \tilde{f} \} + \mathcal{I}_n^N \{ \tilde{f} \} - 2\pi j \sum_i R_{pi} H_n^{(2)}(k_{pi} \rho) k_{pi} \quad (26)$$

where $\mathcal{I}_n^1 \{ \tilde{f} \}$ and $\mathcal{I}_n^N \{ \tilde{f} \}$ now denote integrals around the vertical branch cuts, as illustrated in Fig. 6. Note that the shaded areas are swaths of the improper Riemann sheets swept when the extended real axis path is deformed to wrap around these branch cuts. The summation in (26) includes the poles captured in the deformation, possibly including some on the improper Riemann sheets—the leaky wave poles [52]. Note that if the Sommerfeld pole is located to the left of k_1 —as it would be in the lossy earth case, it is *not* captured and it does not explicitly contribute to the nonspectral representation of the integral. However, due to its close topological proximity to the downward leg of the integration path around k_1 , this pole can still strongly influence the result. In the plasmonic case, this pole is located to the right of k_1 , and is thus included in the residue summation in (26), but it may also strongly influence the branch cut integral.

⁷In this representation, the integration path approaches infinity on an improper Riemann sheet—hence the name. Nevertheless, the integrals converge, as a result of the exponential decay of the Hankel function.

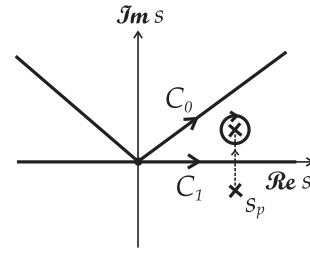


Fig. 7. Illustration of the s -plane in the vicinity of the origin, which corresponds to the branch point k_1 in the k_p -plane.

We will presently address the computation of the branch cut integrals in (26). Hence, upon changing the variable of integration via $k_p = k_1 - js^2$, we express $\mathcal{I}_n^1 \{ \tilde{f} \}$ as [30]

$$\mathcal{I}_n^1 \{ \tilde{f} \} = 2j^{n+1} \sqrt{\frac{2j}{\pi\rho}} e^{-jk_1\rho} \int_0^\infty F(s) e^{-s^2\rho} s ds \quad (27)$$

with

$$F(s) = [\tilde{f}(k_p)] \sqrt{k_p} \mathcal{H}_n(k_p \rho) |_{k_p=k_1-js^2} \quad (28)$$

where $[\tilde{f}(k_p)]$ now represents the jump in $\tilde{f}(k_p)$ as k_{z1} changes sign across the vertical branch cut associated with k_1 , and where we have introduced the normalized Hankel function

$$\mathcal{H}_n(z) \equiv j^{-n} \sqrt{\frac{\pi z}{2j}} e^{jz} H_n^{(2)}(z) \quad (29)$$

which approaches unity for $|z| \rightarrow \infty$. The purpose of this substitution is to make the asymptotic ρ -dependence of the integrand in (27) explicit. The second branch cut integral $\mathcal{I}_n^N \{ \tilde{f} \}$ can similarly be expressed, upon the replacement $k_1 \rightarrow k_N$. As already mentioned in connection with the radial-transmission representation, the contribution from this integral is typically negligible.

In order to correctly evaluate $[\tilde{f}(k_p)]$ in (28), it is required to keep track of the Riemann sheets traversed as the integration in (27) proceeds along the vertical branch cut. This is readily accomplished with reference to Fig. 2. Hence, in the $\Re k_1 < \Re k_N$ case in Fig. 6, we enforce $\Re k_{z1} > 0$ and $\Re k_{zN} > 0$ in computing \tilde{f}^+ (at the left edge of the cut) and reverse the sign of k_{z1} in computing \tilde{f}^- (at the opposite, right edge of the cut). In the $\Re k_1 > \Re k_N$ case, the same rules should be followed in the selection of the k_{z1} branch, but $\Im m k_{zN} < 0$ should be enforced in \tilde{f}^+ and \tilde{f}^- .

The mapping of the k_p -plane into the s -plane introduced in (27) and (28) is illustrated in Fig. 7, where the contours C_0 and C_1 are images of the corresponding paths in Fig. 6 and $s_p = \sqrt{j(k_p - k_1)}$ is the image of the Sommerfeld pole k_p . In the plasmonic case, this pole can cross the real axis and is then captured when the original path C_0 is deformed into the real axis path C_1 . As already mentioned, the Sommerfeld pole may be located arbitrarily close to k_1 —either on the left or on the right of the vertical branch cut—with the attendant spike in the integrand of (27), which makes the integration problematic. In

such a case, the most reliable approach is to extract the contribution of the offending pole from the integrand and to add it back integrated in closed form [24], [55]–[57]. Here, we go one step further and also extract the limit form of the integrand at the branch point, which allows us to express (27) as

$$\mathcal{I}_n^1 \{ \tilde{f} \} = 2j^{n+1} \sqrt{\frac{2j}{\pi\rho}} e^{-jk_1\rho} \cdot \left\{ I_p + \sqrt{\frac{\pi}{\rho}} \left[\frac{F'(0)}{4\rho} - B_p \mathcal{F}(p) \right] \right\} \quad (30)$$

where the integral

$$I_p = \int_0^\infty \left[\frac{F(s)}{s} - F'(0) + \frac{2B_p}{s_p^2} \frac{s^2}{s^2 - s_p^2} \right] e^{-s^2\rho} s^2 ds \quad (31)$$

has a well-behaved integrand and is amenable to numerical quadrature. Here, $F'(0) = \lim_{s \rightarrow 0} F(s)/s$ and is given as

$$F'(0) = \lim_{s \rightarrow 0} \left[\frac{\tilde{f}(k_p)}{s} \right]_{|k_p = k_1 - js^2 \sqrt{k_1} \mathcal{H}_n(k_1\rho)} \quad (32)$$

B_p is the s -plane residue at the pole s_p and is given as

$$B_p = \frac{jR_p}{2s_p} \sqrt{k_p} \mathcal{H}_n(k_p\rho) \quad (33)$$

where R_p is the residue of $\tilde{f}(k_p)$ at the pole k_p

$$\mathcal{F}(p) = 1 + \frac{1}{2p} + j\sqrt{\pi p} [w(\sqrt{p}) - 2e^{-p} U(\Im m s_p)] \quad (34)$$

is the *modified attenuation function*,⁸ where

$$w(z) = e^{-z^2} \operatorname{erfc}(-jz) \quad (35)$$

is the Faddeeva function [60], and

$$p = s_p^2\rho = j(k_p - k_1)\rho \quad (36)$$

is the Sommerfeld *numerical distance* [14, p. 933]. Finally, $U(x)$ is the step function

$$U(x) = \begin{cases} 1, & \text{if } x < 0 \\ \frac{1}{2}, & \text{if } x = 0 \\ 0, & \text{if } x > 0 \end{cases} \quad (37)$$

so that $U(\Im m s_p)$ in (34) is “ON” in the Sommerfeld case, and “OFF” in the plasmonic case. It is interesting that the behavior of the attenuation function is not determined by ρ (or $k_1\rho$) alone, but by the numerical distance parameter p , which also includes the effect of the material constants.⁹ It can be shown that

$$\mathcal{F}(p) \sim -\frac{3}{4p^2}, \quad |p| \gg 1 \quad (38)$$

irrespective of the sign of $\Im m s_p$ [3], [17], [61]. It is important to note that although (34) is discontinuous when the

pole crosses the real axis integration path in Fig. 7—and the Sommerfeld case turns into the plasmonic case—this discontinuity is exactly compensated by the residue¹⁰ term that must now be included in the nonspectral representation (26).

Comparing the three representations, we note that they are all exact, but differ in applicability and efficiency. The axial-transmission representation is the simplest to use, as it does not require pole tracking, and is the only representation applicable for $\rho = 0$, which may be important in certain GPR applications. However, as already mentioned, in surface-field computations where $|z + z'|/\rho \ll 1$, the oscillatory behavior of the Bessel function on the real axis makes it impractical for horizontal ranges exceeding a few hundred wavelengths. The radial-transmission representation also suffers from this limitation, although the interval where oscillations occur is finite. In contrast, the integrands of the nonspectral representation are free of the oscillatory behavior and the rate of convergence actually improves with increasing radial distance ρ . The latter property makes the nonspectral representation ideal for surface-field computations.

D. Asymptotic Surface Field

With the pole-term extracted, this integrand of I_p in (31) is smooth and rapidly decaying, due to the fact that the integration path C_1 is the SDP for $\rho \gg |z + z'|$ [55]. Consequently, I_p in (30) may be neglected for sufficiently large ρ values and—assuming that the second branch cut integral in (26) is also negligible and no poles have been captured in the nonspectral representation—we obtain the closed-form asymptotic expression of the surface field

$$\mathcal{I}_n^1 \{ \tilde{f} \} \approx j^n (2j)^{\frac{3}{2}} \left[\frac{F'(0)}{4\rho} - B_p \mathcal{F}(p) \right] \frac{e^{-jk_1\rho}}{\rho}. \quad (39)$$

This formula has a larger range of applicability than the Sommerfeld–Norton groundwave, but it reduces to the latter in the high-contrast case. The asymptotic form (39) reveals that the Sommerfeld pole is an important factor in the field along the halfspace surface—even when not captured in the nonspectral representation (26). In fact, the exponential term in (34)—along with the other factors that appear in (30)—is exactly the ZW [17]. This ZW, however, is only significant in a limited horizontal range and is cancelled for large ρ , in view of the asymptotic behavior (38) of $\mathcal{F}(p)$.¹¹ In the plasmonic case, where $\Im m s_p > 0$ and the pole is captured and contributes an explicit residue term in (26), its influence may persist over a larger horizontal range, in view of the slowly decaying $\rho^{-\frac{1}{2}}$ amplitude factor of the pole waves—but it also eventually becomes immaterial, due to its exponential decay.

¹⁰Or half-residue, if the pole is exactly on the real axis.

⁸Our $\mathcal{F}(p)$ differs from the Sommerfeld attenuation function [58], [59] in the second term, which is absent in the latter.

⁹Sommerfeld called this the “similarity law of wireless telegraphy” [1].

¹¹As a result of the already mentioned elusive error in the 1909 paper of Sommerfeld [1], there was no asymptotic cancellation of the ZW in his original groundwave formula. Hence, the deleterious effect of this error was that the groundwave seemed to be an important factor in the radio wave propagation along the surface of the earth. It is interesting that Sommerfeld inadvertently arrived at a formula applicable in the plasmonic case. As also noted before, Sommerfeld derived the correct groundwave formula in his 1926 paper [12]—however, he never mentioned or acknowledged the discrepancy with his original expression.

The range dependence of the groundwave (39) is dictated by the numerical distance parameter p and is rather complex. Near the dipole, the dominant behavior is ρ^{-1} , and it evolves into ρ^{-2} dependence with increasing ρ . The $|p| = 1$ point can serve as a demarcation point where the transition from the ρ^{-1} to the ρ^{-2} asymptote begins. It is interesting that the ρ^{-2} asymptotic behavior is in our groundwave formula governed by the limit value of the spectral integrand at the branch point.

For convenience, we will refer to the asymptotic groundwave (39) as the *lateral wave* and the contribution from any proper (top-sheet) pole captured in the nonspectral representation will be called a *trapped wave*.

III. NUMERICAL RESULTS

We include numerical results to illustrate the properties of the alternative field representations and the role of the ZW and SPP. As a suitable representative example, we treat the vector potential (14) due to the vertical dipole. Hence, the Sommerfeld integral of interest here is

$$V = 4\pi \mathcal{S}_0 \left\{ \tilde{f}(k_p) \right\} \quad (40)$$

with

$$\tilde{f}(k_p) = \frac{1 - \vec{I}_1^e}{2jk_{z1}} e^{-jk_{z1}h} = \frac{Z_1^e}{\mathcal{D}^e} \frac{e^{-jk_{z1}h}}{jk_{z1}} \quad (41)$$

where $h = -z' > 0$ and \mathcal{D}^e is the TM dispersion function (15). We focus on the surface field at $z = 0$, and since the direct and image terms in (14) cancel in this case, the vector potential is represented by the Sommerfeld integral alone. In view of (3), the corresponding electric field is as follows [62, p. 391]:

$$E_z \approx -j\omega A_z \approx -j\omega \frac{\mu_1}{4\pi} V \quad (42)$$

where we have neglected the scalar potential contribution, assuming large ρ . For comparison purposes, we also state the corresponding expression for the case of a PEC ground

$$E_z^{PEC} \approx -j\omega \frac{\mu_1}{4\pi} 2 \frac{e^{-jk_1 R}}{R}, \quad R = \sqrt{\rho^2 + h^2}. \quad (43)$$

We assume henceforth that the upper halfspace is air, with the wavenumber $k_1 = k_0 = \omega\sqrt{\mu_0\epsilon_0} = 2\pi/\lambda_0$, where λ_0 is the free space wavelength, and intrinsic impedance $\eta_0 = \sqrt{\mu_0/\epsilon_0}$. The alternative representations require the computation of the poles and, if intercepted, their residues. As already mentioned, in the general multilayer case, the poles k_{pi} can only be determined by the numerical search for the roots of the dispersion function \mathcal{D}^e , and the corresponding residues of $\tilde{f}(k_p)$ in (41) may then be found as¹²

$$R_{pi} = \frac{Z_1}{d\mathcal{D}/dk_p} \frac{e^{-jk_{z1}h}}{jk_{z1}} \Big|_{k_p=k_{pi}}. \quad (44)$$

The evaluation of $d\mathcal{D}/dk_p$ in the above becomes cumbersome beyond two or three layers, hence we use automatic differentiation, which is readily implemented in modern Fortran

¹²Since all impedances pertain to the TM TL network, we henceforth omit the superscripts e for simplicity.

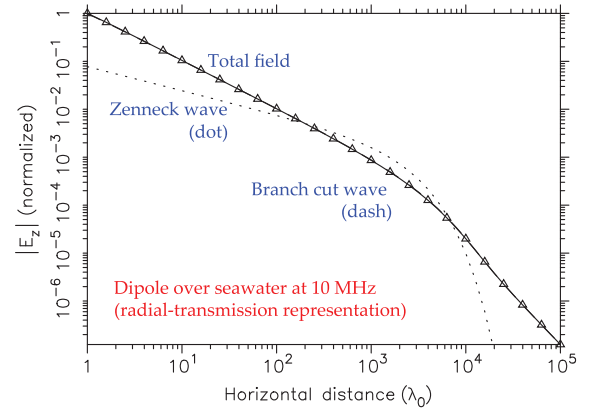


Fig. 8. Radial-transmission representation results for the seawater case. The solid line is the total surface field, including the hyperbolic branch cut contribution and the pole contribution (ZW). The dashed and dotted lines are the branch cut and ZW contributions, respectively.

by operator overloading [63]. When the lower halfspace is homogeneous and thus $\vec{Z}_1 = Z_2$ in (15), the Sommerfeld pole k_p is given by (16) and the residue can easily be found as

$$R_p = -j \frac{\epsilon_r \sqrt{\epsilon_r}}{\epsilon_r^2 - 1} e^{jk_1 h / \sqrt{\epsilon_r + 1}}. \quad (45)$$

The folded $\tilde{f}(k_p)$, also needed in the alternative representations, may be found as

$$[\tilde{f}(k_p)] = \frac{2j}{k_{z1}} \frac{Z_1^2}{\vec{Z}_1^2 - Z_1^2} \left[\cos(k_{z1}h) + j \frac{\vec{Z}_1}{Z_1} \sin(k_{z1}h) \right] \quad (46)$$

where $\Re k_{z1} > 0$, and where we have used the fact that the substitution $k_{z1} \rightarrow -k_{z1}$ implies $Z_1 \rightarrow -Z_1$. The branch point limit form needed to compute $F'(0)$ in (32) readily follows as

$$\lim_{s \rightarrow 0} \frac{[\tilde{f}(k_p)]}{s} \Big|_{k_p=k_1 - js^2} = \left(\frac{2j}{k_1} \right)^{\frac{3}{2}} \frac{1 + jk_1 h \vec{Z}_1}{\vec{Z}_1^2} \quad (47)$$

where $\vec{Z}_1 \equiv \vec{Z}_1/\eta_0|_{k_p=k_1}$, with $\vec{Z}_1 = Z_2$ in the case of a homogeneous lower halfspace.

As the first example, we consider a dipole at $h = 5$ m above seawater with $\epsilon' = 81$ and $\sigma = 4$ S/m at $f = 10$ MHz ($\lambda_0 \approx 30$ m), so that $\epsilon_r = 81 - j7190.04$ and we find the Sommerfeld pole at $k_p/k_1 \approx 0.99999920 - j6.95 \times 10^{-5}$. Hence, this is a high-contrast Sommerfeld case. The radial-transmission and nonspectral representation results for this case are given in Figs. 8 and 9, respectively. In this and other examples that follow, we indicate the benchmark result computed using the partition-extrapolation method along a deformed SIP [64] by triangle symbols. Also, unless otherwise stated, all plots will be normalized to the benchmark result at the initial point. The solid line in Fig. 8 represents the integral around the first *fundamental* branch cut together with the pole contribution (the ZW)—but excluding the second branch cut integral, which is negligible. The dashed line, which is almost indistinguishable from the solid one, represents branch cut integral alone and the dotted line is the ZW contribution alone. The solid line being in good agreement with the benchmark result confirms

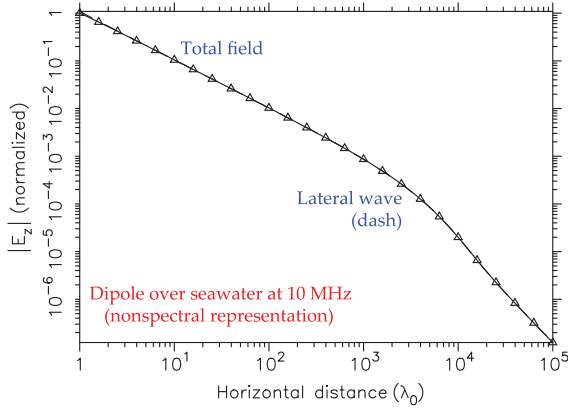


Fig. 9. As in Fig. 8, except the nonspectral representation is used. The solid line is the total surface field, which consists of the vertical branch cut contribution (the ZW is implicit). The dashed line (which is indistinguishable from the solid one) is the lateral wave contribution.

that the second branch cut contribution can indeed be ignored. The ZW initially exhibits the $\rho^{-\frac{1}{2}}$ dependence, but for large enough ρ , the exponential decay dominates. Its influence on the total surface field is only noticeable in the intermediate range, where it exceeds in magnitude the branch cut contribution, but it combines with it destructively, resulting in the total field magnitude that is not much different from that of the branch cut integral. As a result, the total surface field, which is identical to that in Fig. 9, initially follows the ρ^{-1} line, but the rate of decay accelerates farther from the source, eventually reaching the ρ^{-2} asymptote. The $|p| = 1$ knee point corresponds to $\rho/\lambda_0 \approx 2.3 \times 10^3$. Note that in the nonspectral representation the Sommerfeld pole is not captured, and the ZW contribution is implicit. Similar behavior is observed in all Sommerfeld cases we have considered. Consequently, since only the total field is measurable [65], we contend that any attempt to experimentally detect the presence of the ZW in the surface field of a Hertzian dipole is bound to fail. It is well known that a pure ZW can only be excited by a (nonphysical) line dipole of infinite extent [66]. Petrillo *et al.* [2] recently proposed to use a distribution of dipole arrays to enhance the ZW excitation and thus extend the range of maritime surveillance radar.

For the problem above, we next examine the effect of an ice layer ($\epsilon_r = 4$) of thickness $d_2 = d = \lambda_0/50 = 60$ cm on top of the seawater—with the dipole remaining at $h = 5$ m above the ice surface. The numerical search for the roots of the dispersion function (15) yields one pole at $k_p/k_1 \approx 1.0054 - j9.13 \times 10^{-4}$. Hence, with the addition of the ice layer, the Sommerfeld pole has migrated to the right and crossed the vertical branch cut line emanating from k_1 .¹³ The associated wave is a dielectric waveguide mode, trapped by the subwavelength lossless slab backed by a lossy conductor. Since $\Im m s_p > 0$ in this case, we have a situation akin to the plasmonic case, where the exponential term in the attenuation function (34) is absent and an explicit residue is included in the nonspectral representation (26). As the results in Fig. 10 demonstrate, the field behavior is

¹³This pole crossing, which signifies that the ZW becomes a trapped mode, occurs with the addition of even an extremely thin, say 1 mm, ice layer. For $d = 30$ cm, $k_p/k_1 \approx 1.0015 - j4.73 \times 10^{-4}$.

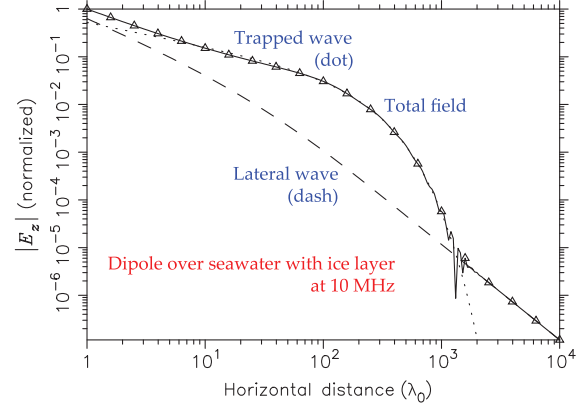


Fig. 10. Nonspectral representation results for the seawater case with a 60-cm ice layer. The solid line is the total surface field, including the vertical branch cut contribution and the trapped wave. The dashed and dotted lines are the lateral wave and trapped wave contributions, respectively.

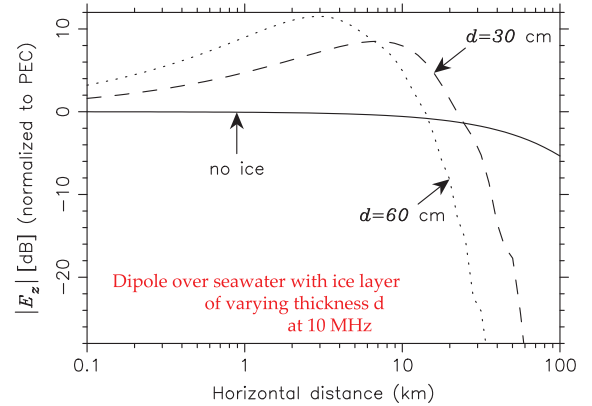


Fig. 11. Effect of ice layer of varying thickness d over seawater.

now dominated over a wide range by the trapped wave with the inverse-square-root ρ -dependence, until the exponential decay factor makes it eventually fall below the lateral wave contribution, which decays as ρ^{-2} for $|p| \gg 1$. The wiggles observed near the point of intersection of the lateral wave and the trapped wave contributions are due to the interference between these waves when their magnitudes become comparable.

Continuing with this example in Fig. 11, we compare the nonspectral representation results for an ice layer of varying thickness, with the dipole at the ice surface ($h = 0$). In this particular case, the plots are normalized to $|E_z^{PEC}|$, which behaves asymptotically as ρ^{-1} , and the horizontal range is 100 km. The positive slope of the curves indicate that the rate of decay is in that range slower than inverse- ρ , which is the effect of the trapped wave. This effect is enhanced with increasing ice thickness, but the exponential decay of the groundwave then also increases, because the trapped wave becomes more closely bound to the lossy seawater surface. The results in Fig. 11 are in excellent agreement with those of Mahmoud and Antar [3].

The next example pertains to GPR detection of leaking pipes in the shallow subsurface at $f = 100$ MHz ($\lambda_0 = 3$ m) [4]. The lower halfspace layers are dry sand ($\epsilon_r = 4$, thickness $d_2 = 1$ m), air gap (thickness $d_3 = 10$ cm), and water-logged soil ($\epsilon' = 80$, $\sigma = 4$ S/m). The vertical dipole is in air at the

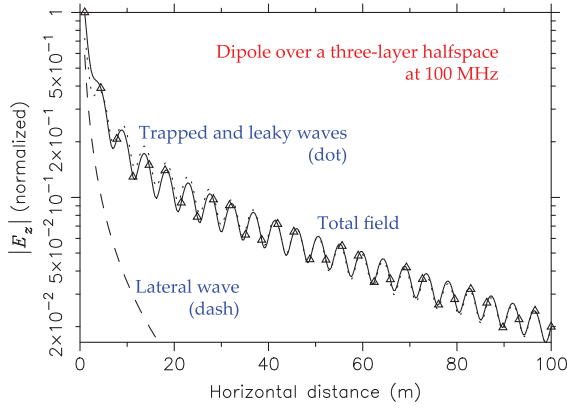


Fig. 12. Nonspectral representation results for the three-layer halfspace GPR example. The solid line is the total surface field, including the vertical branch cut contribution and the pole waves. The dashed and dotted lines are the lateral wave and pole wave (trapped and leaky) contributions, respectively.

TABLE I
POLES INCLUDED IN THE GPR EXAMPLE

k_{pi}/k_1	Riemann Sheet
$1.0254 - j 6.1701 \times 10^{-3}$	I
$1.6783 - j 6.7940 \times 10^{-3}$	I
$0.49827 - j 0.64828$	II
$0.17116 - j 2.5072$	II
$0.14115 - j 4.1411$	II

upper surface ($h = 0$) and that is where the field is observed. The nonspectral representation results for this case are plotted in Fig. 12 and the poles that were included are listed in Table I. There are two surface waves trapped by the sand bar and their interference creates the undulations. The first pole in Table I is close to the branch point and we treat it as the Sommerfeld pole in the formulation of this problem. The lateral wave is seen to be negligible, except near the source, and the trapped waves dominate in the moderate horizontal range. To bring the nonspectral representation result in agreement with the benchmark, the contributions from three leaky-wave poles, also captured by the deformed integration path, had to be included. These waves are heavily damped, but contribute significantly in the vicinity of the dipole.

We next consider a dipole at $f = 0.5$ THz ($\lambda_0 \approx 600 \mu\text{m}$) located at $h = 5 \mu\text{m}$ above aluminum (Al) ($\epsilon_r = -3.3 \times 10^4 - j 1.273 \times 10^6$) halfspace [67]. The Sommerfeld pole is found at $k_p/k_1 \approx 1.00000001 - j 3.9262 \times 10^{-7}$ and is thus captured in the nonspectral representation, for which the results are given in Fig. 13.¹⁴ Note that this is a high-contrast plasmonic case with $\epsilon'' \gg |\epsilon'|$. The SPP contribution to the total surface field is seen to be insignificant and the knee corresponding to the $|p| = 1$ demarcation point begins at $\rho/\lambda_0 \approx 4 \times 10^4$ (or 243 m).

Next, for the example above, we examine the effect of a polyethylene-coating layer ($\epsilon_r = 2.25$, thickness $d_2 = \lambda_0/50 = 12.5 \mu\text{m}$) [67]. The pole is now found at $k_p/k_1 \approx 1.0027 - j 4.5887 \times 10^{-5}$ and it contributes a trapped wave. The

¹⁴It was not practical here to compute the benchmark result using the SIP beyond $\rho/\lambda_0 = 10^5$.

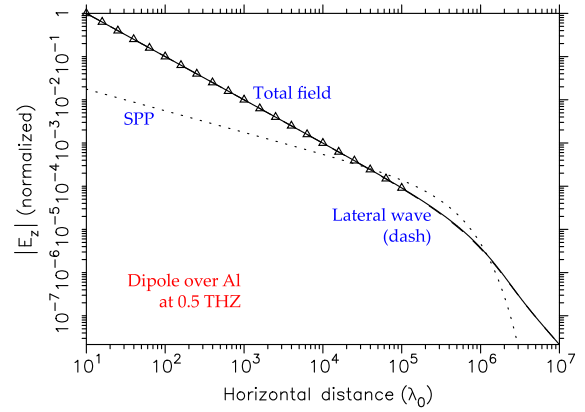


Fig. 13. Nonspectral representation results for the THz Al case. The solid line is the total surface field, including the vertical branch cut contribution and the SPP. The dashed and dotted lines are the lateral wave and SPP contributions, respectively.

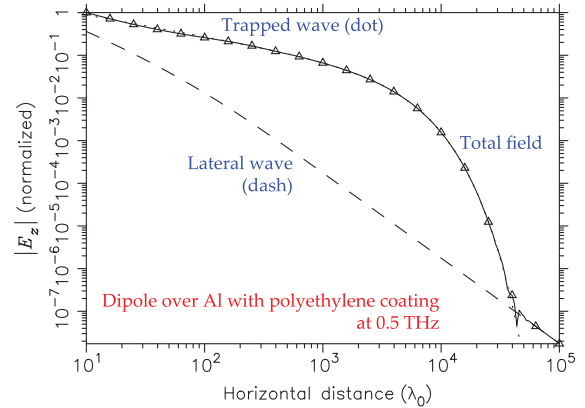


Fig. 14. As in Fig. 13, except Al is coated with a thin, lossless polyethylene layer. The solid line is the total surface field, including the vertical branch cut contribution and the trapped wave. The dashed and dotted lines are the lateral wave and trapped wave contributions, respectively.

nonspectral representation results plotted in Fig. 14 indicate that the surface field behavior is dominated over a wide range by the trapped wave with the inverse-square-root ρ -dependence, until the exponential decay factor makes it fall below the lateral wave, which is in transition to the ρ^{-2} asymptote. This wave is much more tightly bound to the surface than the SPP in the corresponding bare Al case of Fig. 13.¹⁵

As the next example, we consider a dipole placed at $h = 10$ nm over silver (Ag) at $\lambda_0 = 0.852 \mu\text{m}$. By curve-fitting the tabulated data [68], we find the corresponding dielectric constant of Ag as $\epsilon_r = -36.9336 - j 0.4259$ and the Sommerfeld pole at $k_p/k_1 \approx 1.0138 - j 1.6264 \times 10^{-4}$, which is thus captured in the nonspectral representation, for which we present the results in Fig. 15. Note that this is also a high-contrast plasmonic case, but with $\epsilon'' \ll |\epsilon'|$, which means that the SPP has the properties of a low-loss Fano wave [69]. The results in Fig. 15 show that the field behavior is dominated over a wide range by the Fano wave with the inverse-square-root ρ -dependence, until the exponential decay factor makes it eventually fall off below the lateral

¹⁵Gong *et al.* [67] call this phenomenon the “THz surface wave collapse.” Note that they refer to the SPP as the “Zenneck THz surface wave.”

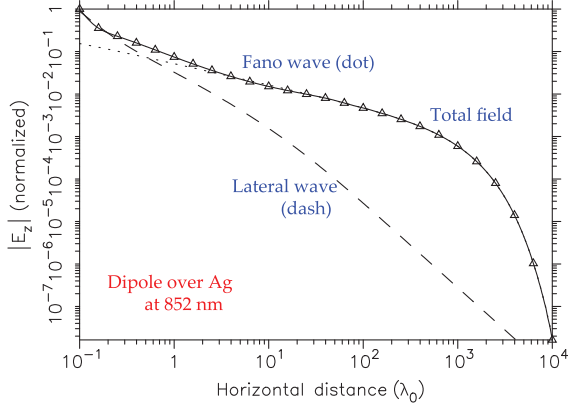


Fig. 15. Nonspectral representation results for the near-infrared Ag case. The solid line is the total surface field, including the vertical branch cut contribution and the pole (Fano) wave). The dashed and dotted lines are the lateral wave and Fano wave contributions, respectively.

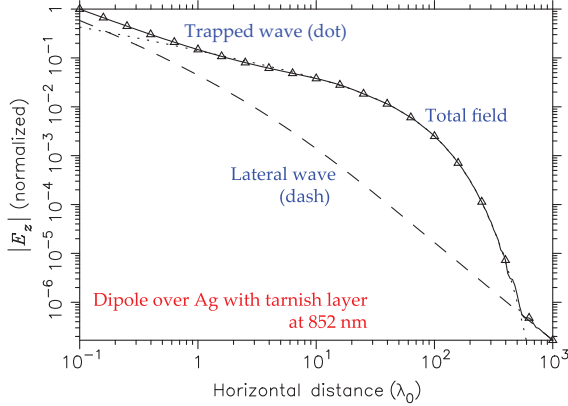


Fig. 16. As in Fig. 15, except that Ag is coated with a thin Ag_2S tarnish layer. The solid line is the total surface field, including the vertical branch cut contribution and the trapped wave. The dashed and dotted lines are the lateral wave and trapped wave contributions, respectively.

wave, which decays as ρ^{-2} . Incidentally, the $|p| = 1$ knee point now corresponds to $\rho/\lambda_0 \approx 11.5$ (or $\approx 10 \mu\text{m}$).

When silver is exposed to air, a thin silver sulfide (Ag_2S) layer builds up, which modifies the surface wave behavior [70]. This is confirmed by the results of Fig. 16, which are for the same case as above, except that an Ag_2S tarnish layer of thickness 12 nm has been added on top of Ag. By fitting the tabulated dielectric function of Ag_2S , we find $\epsilon_r = 8.425 - j1.333$ [57], and the numerical pole search yields $k_p/k_1 \approx 1.0388 - j2.7894 \times 10^{-3}$. This pole is captured in the nonspectral representation and it contributes a trapped wave. Comparing the results of Figs. 15 and 16, we note the approximately fivefold reduction of the SPP range in the presence of the tarnish layer, which is not lossless.

As the last example, in Fig. 18, we present nonspectral representation results for a vertical dipole located at $h = 100$ nm above chromium (Cr) halfspace. Here, unlike in all previous cases, the field is observed at a fixed distance $\rho = 5 \mu\text{m}$ from the dipole, as the frequency (photon energy) varies in the near-infrared band. In this frequency range, the real part ϵ' of the dielectric function of Cr passes from negative to positive and

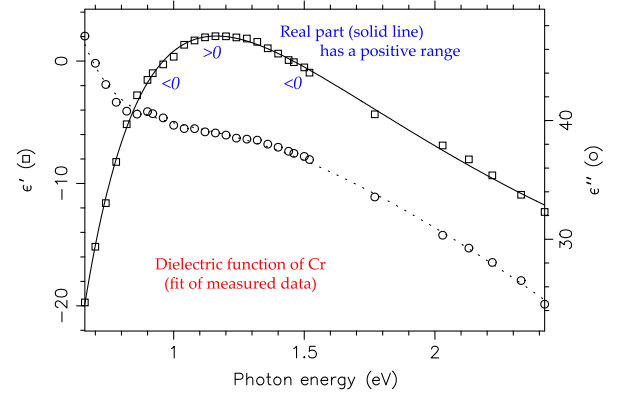


Fig. 17. Dielectric function of chromium, showing a range of positive ϵ' .

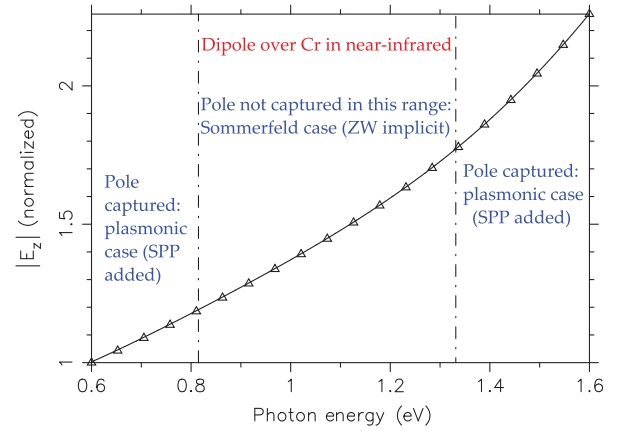


Fig. 18. Nonspectral representation results for the near-infrared Cr case. The total surface field is plotted versus photon energy at a fixed observation point.

back [71], as indicated in Fig. 17, where the experimental data are fitted to a partial-fraction model [68]. Hence, as the Sommerfeld pole migrates due to the changing frequency, there is a transition from the plasmonic case (the pole is captured and contributes a SPP) to the Sommerfeld case (the pole is not captured, but the ZW is implicit in the groundwave) and back. We note that the total field plot in Fig. 18 is continuous, even though the pole residue is only included in the SPP ranges. Hence, the field discontinuities at the points where the SPP is turned OFF and ON are exactly compensated by the ZW implicit in the attenuation function. This last example clearly demonstrates the close relationship between the ZW and SPP.

IV. CONCLUSION

We have presented a new look at the classical Sommerfeld problem, with an extension to multilayer and plasmonic media. In particular, we have shown that the surface field admits alternative representations—termed axial-transmission, radial-transmission, and nonspectral. In the lossy conductor case, the spectral integrands possess a pole on the proper Riemann sheet, which is always captured in the radial-transmission representation and it contributes the ZW. In the nonspectral representation, the pole is captured in the plasmonic case ($\epsilon' < 0$), where it contributes the SPP, but not in the Sommerfeld case ($\epsilon' > 0$), where it contributes an implicit ZW, which is asymptotically

cancelled in the total surface field. The appearance or not of the ZW in a particular field representation does not prove or disprove the “existence” or “physical reality” of this wave. The ZW is always a part of the total field representation—explicitly or implicitly, but it never dominates and cannot be experimentally detected in the surface field of a Hertzian dipole. The horizontal range behavior of the surface field is dictated by the “numerical distance” parameter p , which depends both on ρ and the media parameters. Unless the SPP is strongly excited (Fano wave), the surface field decay rate is ρ^{-1} near the dipole, but is always ρ^{-2} for $|p| \gg 1$, with the transition point (knee) given by the condition $|p| \approx 1$. The ZW and SPP are closely related and one may evolve into the other with the change of frequency. In the layered halfspace case, the waves trapped in the low-loss layers may dominate the surface field behavior in the near and intermediate horizontal ranges, similar to the Fano wave in the plasmonic case.

REFERENCES

- [1] A. Sommerfeld, “Über die Ausbreitung der Wellen in der drahtlosen Telegraphie,” *Ann. d. Phys.*, vol. 28, pp. 665–736, 1909.
- [2] L. Petrillo, F. Jangal, M. Darces, J.-L. Montmagnon, and M. Hélier, “Towards a better excitation of the surface wave,” *Prog. Electromagn. Res. M*, vol. 13, pp. 17–28, 2010.
- [3] S. F. Mahmoud and Y. M. M. Antar, “High frequency ground wave propagation,” *IEEE Trans. Antennas Propag.*, vol. 62, no. 11, pp. 5841–5846, Nov. 2014.
- [4] J. D. Cross and P. R. Atkins, “Electromagnetic propagation in four-layered media due to a vertical electric dipole: A clarification,” *IEEE Trans. Antennas Propag.*, vol. 63, no. 2, pp. 866–870, Feb. 2015.
- [5] T.-I. Jeon and D. Grischkowsky, “THz Zenneck surface wave (THz surface plasmon) propagation on a metal sheet,” *Appl. Phys. Lett.*, vol. 88, no. 6, p. 061113-1–061113-3, 2006.
- [6] L. Novotny, “Allowed and forbidden light in near-field optics. I. A single dipolar light source,” *J. Opt. Soc. Amer. A*, vol. 14, no. 1, pp. 91–104, 1997.
- [7] B. Ung and Y. Sheng, “Optical surface waves over metallo-dielectric nanostructures: Sommerfeld integrals revisited,” *Opt. Express*, vol. 16, no. 12, pp. 9073–9086, 2008.
- [8] J. Zenneck, “Über die Fortpflanzung ebener elektromagnetischer Wellen längs einer ebenen Leiterfläche und ihre Beziehung zur drahtlosen Telegraphie,” *Ann. Phys.*, vol. 23, pp. 846–866, 1907.
- [9] L. B. Felsen, “Alternative Green’s function representations for a grounded dielectric slab,” in *Onde Superficiali: Lectures Given at the Centro Internazionale Matematico Estivo (C.I.M.E.), Varenna (Como), Italy, September 4–13, 1961*, G. Toraldo di Francia, Ed. New York, NY, USA: Springer, 2011, pp. 191–219.
- [10] K. A. Norton, “Propagation of radio waves over a plane earth,” *Nature*, vol. 135, no. 3423, pp. 954–955, 1935.
- [11] K. F. Niessen, “Zur Entscheidung zwischen den beiden Sommerfeldschen Formeln für die Fortpflanzung von drahtlosen Telegraphie,” *Ann. d. Phys. 5. Folge*, vol. 29, pp. 585–596, 1937.
- [12] A. Sommerfeld, “Über die Ausbreitung der Wellen in der drahtlosen Telegraphie,” *Ann. d. Phys.*, vol. 81, pp. 1135–1153, 1926.
- [13] H. Weyl, “Ausbreitung elektromagnetischer Wellen über einem ebenem Leiter,” *Ann. Phys.*, vol. 365, no. 21, pp. 481–500, 1919.
- [14] A. Sommerfeld, “Drahtlose Telegraphie,” in *Die Differential- und Integralgleichungen der Mechanik und Physik, Part II*, P. Frank and R. von Mises, Eds., 2nd ed. New York, NY, USA: Rosenberg, 1943, ch. 23, pp. 918–977.
- [15] J. Grosskopf, “Das Strahlungsfeld eines vertikalen Dipolenders über geschichtetem Boden,” *Hochfrequenztech. Elektroakustik*, vol. 60, pp. 136–141, Nov. 1942.
- [16] J. R. Wait, “Radiation from a vertical electric dipole over a stratified ground,” *IRE Trans. Antennas Propag.*, vol. AP-1, no. 1, pp. 9–11, Jul. 1953.
- [17] J. R. Wait, “Excitation of surface waves on conducting, stratified, dielectric-clad, and corrugated surfaces,” *J. Res. Natl. Bur. Stand.*, vol. 59, no. 6, pp. 365–377, Dec. 1957.
- [18] K. A. Norton, “The propagation of radio waves over the surface of the earth and in the upper atmosphere—Part II: The propagation from vertical, horizontal, and loop antennas over a plane earth of finite conductivity,” *Proc. IRE*, vol. 25, no. 9, pp. 1203–1237, Sep. 1937.
- [19] B. van der Pol, “Theory of the reflection of the light from a point source by a finitely conducting flat mirror, with an application to radiotelegraphy,” *Physica*, vol. 2, no. 1–12, pp. 843–853, 1935.
- [20] J. R. Wait, “The ancient and modern history of EM ground-wave propagation,” *IEEE Antennas Propag. Mag.*, vol. 40, no. 5, pp. 7–24, Oct. 1998.
- [21] T. S. M. Maclean and Z. Wu, *Radiowave Propagation Over Ground*. London, U.K.: Chapman & Hall, 1993.
- [22] J. D. Milsom, “Surface waves, and sky waves below 2 MHz,” in *Propagation of Radiowaves*, M. P. M. Hall, L. W. Barclay, and M. T. Hewitt, Eds. London, U.K.: Inst. Elect. Eng., 1996, ch. 15, pp. 307–334.
- [23] R. W. P. King and S. S. Sandler, “The electromagnetic field of a vertical electric dipole over the earth or sea,” *IEEE Trans. Antennas Propag.*, vol. 42, no. 3, pp. 382–389, Mar. 1994.
- [24] R. E. Collin, “Hertzian dipole radiating over a lossy earth or sea: Some early and late 20th-century controversies,” *IEEE Antennas Propag. Mag.*, vol. 46, no. 2, pp. 64–79, Apr. 2004.
- [25] M. Cardona, “Fresnel reflection and surface plasmons,” *Amer. J. Phys.*, vol. 39, no. 10, p. 1277, 1971.
- [26] A. Sihvola, J. Qi, and I. V. Lindell, “Bridging the gap between plasmonics and Zenneck wave,” *IEEE Antennas Propag. Mag.*, vol. 52, no. 1, pp. 124–136, Feb. 2010.
- [27] C. H. Gan, L. Lalouat, P. Lalanne, and L. Aigouy, “Optical quasicylindrical waves at dielectric interfaces,” *Phys. Rev. B*, vol. 83, pp. 085 422-1–085 422-6, 2011.
- [28] K. A. Michalski and J. R. Mosig, “Multilayered media Green’s functions in integral equation formulations (invited review paper),” *IEEE Trans. Antennas Propag.*, vol. 45, pp. 508–519, Mar. 1997.
- [29] K. A. Michalski, “Electromagnetic field computation in planar multilayers,” in *Encyclopedia of RF and Microwave Engineering*, vol. 2, K. Chang, Ed. Hoboken, NJ, USA: Wiley, 2005, pp. 1163–1190.
- [30] J. R. Wait, “Asymptotic theory for dipole radiation in the presence of a lossy slab lying on a conducting half-space,” *IEEE Trans. Antennas Propag.*, vol. AP-15, no. 5, pp. 645–648, Sep. 1967.
- [31] A. Baños, *Dipole Radiation in the Presence of a Conducting Half-Space*. New York, NY, USA: Pergamon, 1966.
- [32] A. Hessel, “General characteristics of traveling-wave antennas,” in *Antenna Theory-Part 2*, R. E. Collin and F. J. Zucker, Eds. New York, NY, USA: McGraw-Hill, 1969, ch. 19, pp. 151–258.
- [33] R. Mittra and S. W. Lee, *Analytical Techniques in the Theory of Guided Waves*. New York, NY, USA: Macmillan, 1971.
- [34] T. D. Visser, H. Blok, and D. Lenstra, “Modal analysis of planar waveguide with gain and losses,” *IEEE J. Quantum Electron.*, vol. 31, no. 10, pp. 1803–1810, Oct. 1995.
- [35] A. Ishimaru, J. R. Thomas, and S. Jaruwatanadilok, “Electromagnetic waves over half-space metamaterials of arbitrary permittivity and permeability,” *IEEE Trans. Antennas Propag.*, vol. 53, no. 3, pp. 915–921, Mar. 2005.
- [36] A. Sommerfeld, *Partial Differential Equations in Physics*, vol. VI. New York, NY, USA: Academic, 1949.
- [37] C. T. Tai, “The effect of a grounded slab on the radiation from a line source,” *J. Appl. Phys.*, vol. 22, no. 4, pp. 405–414, 1951.
- [38] A. Ishimaru, *Electromagnetic Wave Propagation, Radiation, and Scattering*. Englewood Cliffs, NJ, USA: Prentice-Hall, 1991.
- [39] W. L. Weeks, *Electromagnetic Theory for Engineering Applications*. Hoboken, NJ, USA: Wiley, 1964.
- [40] R. E. Smith, S. N. Houde-Walter, and G. W. Forbes, “Mode determination for planar waveguides using the four-sheeted dispersion relation,” *IEEE J. Quantum Electron.*, vol. 28, no. 6, pp. 1520–1526, Jun. 1992.
- [41] A. V. Kukulshin, “On the existence conditions for a fast surface wave,” *Phys. Usp.*, vol. 55, no. 11, pp. 1124–1133, 2012.
- [42] V. V. Shevchenko, “Surface electromagnetic waves on the plain boundaries of electroconductive media of high conductivity, Zenneck’s wave (in Russian),” *J. Radio Electron.*, no. 7, pp. 1–19, 2013.
- [43] L. M. Delves and J. N. Lyness, “A numerical method for locating the zeros of an analytic function,” *Math. Comput.*, vol. 21, pp. 543–560, Oct. 1967.
- [44] P. Kravanja, M. Van Barel, O. Ragos, M. N. Vrahatis, and F. A. Zafiroopoulos, “ZEAL: A mathematical software package for computing zeros of analytic functions,” *Comput. Phys. Commun.*, vol. 124, pp. 212–232, 2000.

- [45] L. Knockaert, H. Rogier, and D. De Zutter, "An FFT-based signal identification approach for obtaining the propagation constants of the leaky modes in layered media," *Int. J. Electron. Commun. (AEÜ)*, vol. 59, pp. 230–238, 2005.
- [46] R. E. Smith and S. N. Houde-Walter, "The migration of bound and leaky solutions to the waveguide dispersion relation," *J. Lightwave Technol.*, vol. 11, pp. 1760–1768, Nov. 1993.
- [47] A. Bakhtazad, H. Abiri, and R. Ghayour, "A general transform for regularizing planar open waveguide dispersion relation," *J. Lightwave Technol.*, vol. 15, no. 2, pp. 383–390, Feb. 1997.
- [48] R. Rodríguez-Berral, F. Mesa, and F. Medina, "Appropriate formulation of the characteristic equation for open nonreciprocal layered waveguides with different upper and lower half-spaces," *IEEE Trans. Microw. Theory Techn.*, vol. 53, no. 5, pp. 1613–1623, May 2005.
- [49] A. G. Polimeridis, T. V. Yioultsis, and T. D. Tsiboukis, "An efficient pole extraction technique for the computation of Green's functions in stratified media using a sine transformation," *IEEE Trans. Antennas Propag.*, vol. 55, no. 1, pp. 227–229, Jan. 2007.
- [50] F. W. J. Olver, D. W. Lozier, R. F. Boisvert, and C. W. Clark, Eds., *NIST Handbook of Mathematical Functions*. Cambridge, U.K.: Cambridge Univ. Press, 2010.
- [51] S. Barkeshli and P. H. Pathak, "Radial propagation and steepest-descent path integral representations of the planar microstrip dyadic Green's function," *Radio Sci.*, vol. 25, pp. 161–174, Mar./Apr. 1990.
- [52] T. Tamir and A. A. Oliner, "Guided complex waves. Part 1. Fields at an interface," *Proc. IEE*, vol. 110, no. 2, pp. 310–324, Feb. 1963.
- [53] W. M. Ewing, W. S. Jardetzky, and F. Press, *Elastic Waves in Layered Media*. New York, NY, USA: McGraw-Hill, 1957.
- [54] J. R. Mosig and A. A. Melcón, "Green's functions in lossy layered media: Integration along the imaginary axis and asymptotic behavior," *IEEE Trans. Antennas Propag.*, vol. 51, no. 12, pp. 3200–3208, Dec. 2003.
- [55] K. A. Michalski, "On the efficient evaluation of integrals arising in the Sommerfeld halfspace problem," in *Moment Methods in Antennas and Scatterers*, R. C. Hansen, Ed. Norwood, MA, USA: Artech House, 1990, pp. 325–331, (reprinted from *IEE Proc. Pt. H Microw. Opt. Antennas*, vol. 132, pp. 213–218, Aug. 1985).
- [56] F. Mesa, R. R. Boix, and F. Medina, "Closed-form expressions of multi-layered planar Green's functions that account for the continuous spectrum in the far field," *IEEE Trans. Microw. Theory Techn.*, vol. 56, no. 7, pp. 1601–1614, Jul. 2008.
- [57] R. D. Nevels and K. A. Michalski, "On the behavior of surface plasmons at a metallo-dielectric interface," *J. Lightwave Technol.*, vol. 32, pp. 3299–3305, Oct. 2014.
- [58] J. R. Wait, "Electromagnetic surface waves," in *Advances in Radio Research*, vol. 1, J. A. Saxton, Ed. New York, NY, USA: Academic, 1964, pp. 157–217.
- [59] S. Christiansen, "Computation of Sommerfeld's attenuation function," *Apl. Mat.*, vol. 18, no. 5, pp. 379–384, 1973.
- [60] G. P. M. Poppe and C. M. J. Wijers, "More efficient computation of the complex error function," *ACM Trans. Math. Software*, vol. 16, no. 1, pp. 38–46, 1990.
- [61] L. E. Vogler, "A note on the attenuation function for propagation over flat layered ground," *IEEE Trans. Antennas Propag.*, vol. 12, no. 2, pp. 240–242, Mar. 1964.
- [62] J. R. Wait, "Characteristics of antennas over lossy earth," in *Antenna Theory-Part 2*, R. E. Collin and F. J. Zucker, Eds. New York, NY, USA: McGraw-Hill, 1969, ch. 23, pp. 386–437.
- [63] A. Markus, *Modern Fortran in Practice*. Cambridge, U.K.: Cambridge Univ. Press, 2012.
- [64] K. A. Michalski, "Extrapolation methods for Sommerfeld integral tails (Invited review paper)," *IEEE Trans. Antennas Propag.*, vol. 46, no. 10, pp. 1405–1418, Oct. 1998.
- [65] Yu. B. Bashkuev, V. B. Khaptanov, and M. G. Dembelov, "Experimental proof of the existence of a surface electromagnetic wave," *Tech. Phys. Lett.*, vol. 36, no. 2, pp. 136–139, 2010.
- [66] G. Goubau, "Über die Zennecksche Bodenwelle," *Z. angew. Phys.*, vol. 3, no. 3/4, pp. 103–107, 1951.
- [67] M. Gong, T.-I. Jeon, and D. Grischkowsky, "THz surface wave collapse on coated metal surfaces," *Opt. Express*, vol. 17, no. 19, pp. 17 088–17 101, 2009.
- [68] K. A. Michalski, "On the low-order partial-fraction fitting of dielectric functions at optical wavelengths," *IEEE Trans. Antennas Propag.*, vol. 61, no. 12, pp. 6128–6135, Dec. 2013.
- [69] E. Burstein, A. Hartstein, J. Schoenewald, A. A. Maradudin, D. L. Mills, and R. F. Wallis, "Surface polaritons—Electromagnetic waves at interfaces," in *Polaritons: Proc. 1st Taormina Res. Conf. Struct. Matter*, Taormina, Italy, Oct. 2–6, 1972, (reprints of selected key papers from the literature, E. Burstein and F. De Martini, Eds. New York, NY, USA: Pergamon, 1974, pp. 89–108).
- [70] P. Lalanne and J. P. Hugonin, "Interaction between optical nano-objects at metallo-dielectric interfaces," *Nat. Phys.*, vol. 2, pp. 551–556, Aug. 2006.
- [71] M. Sarrazin and J.-P. Vigneron, "Light transmission assisted by Brewster-Zennek modes in chromium films carrying a subwavelength hole array," *Phys. Rev. B*, vol. 71, pp. 075404-1–075404-5, 2005.

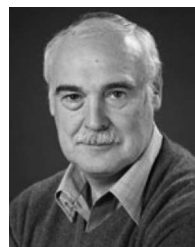


Krzysztof A. Michalski (S'78–M'81–SM'88–F'01) received the M.Sc. degree from Wrocław Technological University, Wrocław, Poland, in 1974, and the Ph.D. degree from the University of Kentucky, Lexington, KY, USA, in 1981, both in electrical engineering.

From 1982 to 1986, he was with the University of Mississippi, Oxford, MS, USA, and since 1987, he has been with Texas A&M University, College Station, TX, USA. In the course of the years past, he also held Visiting Professorships with École

Polytechnique Fédérale de Lausanne (multiple times), Texas A&M University, Qatar, Université de Nice-Sophia Antipolis, Nice, France, Universitat Politècnica de Catalunya, Barcelona, Spain, and Technische Universität München, Munich, Germany, and was a Visiting Scientist at Sandia National Laboratories, Albuquerque, NM, USA, and the National Institute of Standards and Technology, Gaithersburg, MD, USA. His research interests include electromagnetic theory and computational electromagnetics, with emphasis on Green function methods and layered media problems.

Dr. Michalski was Technical Program Chair of the 2002 IEEE Antennas and Propagation Society International Symposium. He was the recipient of the Best EMP Paper Award from the SUMMA Foundation, USA, in 1984, the Oliver Lodge Premium from the IEE, U.K., in 1986, and the Sergei A. Schelkunoff Transactions Prize Paper Award from the IEEE Antennas and Propagation Society in 2015.



Juan R. Mosig (S'76–M'87–SM'94–F'99) was born in Cádiz, Spain. He received the degree in electrical engineering from the Universidad Politécnica de Madrid, Madrid, Spain, in 1973, and the Ph.D. degree in electrical engineering from the École Polytechnique Fédérale de Lausanne (EPFL), Lausanne, Switzerland, in 1983.

Since 1991, he has been a Professor with the Laboratory of Electromagnetics and Acoustics (LEMA), EPFL, and has been its Director since 2000. He has held scientific appointments with

the Rochester Institute of Technology, Rochester, NY, USA; the Syracuse University, Syracuse, NY, USA; the University of Colorado at Boulder, CO, USA; University of Rennes, Rennes, France; University of Nice, Nice, France; and the Technical University of Denmark, Lyngby, Denmark. He has authored four chapters in books on microstrip antennas and circuits and over 150 reviewed papers. His research interests include electromagnetic theory, numerical methods, and planar antennas.

Dr. Mosig has been the Swiss Delegate for European COST Antenna Actions since 1985 and the Chair for the two last Actions 284 and IC0603 ASSIST from 2003 to 2011. From 2004 to 2007, he was Vice-Coordinator of the FP6 Network of Excellence ACE, that enabled the EuCAP Conference series. He has also served as Member of the Board in the Coordination Actions ARTIC (FP6) and CARE (FP7) and Transnational Delegate in the IEEE APS AdCom. He is a Founding Member and Chair of the European Association on Antennas and Propagation (EurAAP) and also chairs the EuCAP Conferences series and its Steering Committee. He also founded (2006) and conducted the series of INTELECT International Workshops on Computational Electromagnetics. He was the recipient of the 2015 IEEE Antennas and Propagation Society Sergei A. Schelkunoff Transactions Prize Paper Award.